PHYSICAL REVIEW D **84,** 063515 (2011)

Complete WMAP constraints on band-limited inflationary features

Cora Dvorkin[1,2] and Wayne Hu[1,3]

[1]*Kavli Institute for Cosmological Physics, Enrico Fermi Institute, University of Chicago, Chicago, Illinois 60637, USA*
[2]*Department of Physics, University of Chicago, Chicago, Illinois 60637, USA*
[3]*Department of Astronomy & Astrophysics, University of Chicago, Chicago, Illinois 60637, USA*

(Received 22 June 2011; published 15 September 2011)

Using a principal component basis that accommodates order unity features in the slow-roll parameters as fine as $1/10$ of a decade across more than 2 decades of the inflationary expansion, we test slow-roll and single-field inflation with the WMAP7 data. Detection of any nonzero component would represent a violation of ordinary slow roll and indicate a feature in the inflaton potential or sound speed. Although one component shows a deviation at the 98% CL, it cannot be considered statistically significant given the 20 components tested. The maximum likelihood principal component parameters only improve $2\Delta \ln L$ by 17 for the 20 parameters associated with known glitches in the WMAP power spectrum at multipoles $\ell < 60$. We make model-independent predictions for the matching glitches in the polarization spectrum that would test their inflationary origin. This complete analysis for band-limited features in the source function of generalized slow roll can be used to constrain parameters of specific models of the inflaton potential without requiring a separate likelihood analysis for each choice. We illustrate its use by placing bounds on the height and width of a steplike feature in the potential proposed to explain the glitch at $20 \leq \ell \leq 40$. Even allowing for the presence of features in the temperature spectrum, single-field inflation makes sharp falsifiable predictions for the acoustic peaks in the polarization whose violation would require extra degrees of freedom.

DOI: 10.1103/PhysRevD.84.063515 PACS numbers: 98.80.−k, 98.70.Vc, 98.80.Cq, 98.80.Es

I. INTRODUCTION

Observed glitches in the WMAP power spectrum of cosmic microwave background (CMB) temperature fluctuations [1], such as the low quadrupole and the dip and bump at $\ell = 20$–40, have motivated many studies of features in the initial conditions. Most of these studies have focused on the reconstruction of the curvature power spectrum through parametric, minimally parametric or regularized inverse techniques (e.g. [2–12]).

Reconstruction of the curvature spectrum suffers from two potential problems. Given that fine scale features are observable at high wave number, parametric models are not complete unless a very large number of parameters are employed. Secondly, not all curvature power spectra can arise from physical mechanisms in the early universe making parametric models potentially overcomplete and subject to fitting the noise instead of fitting the physics. For example, a delta function in the initial curvature spectrum would be highly observable but not expected to arise in any physical model.

For the purposes of testing inflationary models of the initial conditions one can instead try to constrain the shape of the inflaton potential under the assumption that inflation arises from a single scalar field with a canonical kinetic term. Specific potentials have been used to test the origin of the low quadrupole moment, the glitches at multipole moments $\ell = 20$–40 and glitches near the WMAP beam scale [1,13–15]. On the other hand, model-independent reconstruction approaches have implicitly or explicitly assumed a slowly varying inflaton potential [16–20].

Sharp features in the inflaton potential would cause features in the temperature power spectrum [21,22]. As long as those features are of small amplitude, inflation continues uninterrupted but certain slow-roll parameters are neither constant nor necessarily small. The generalized slow roll (GSR) approach [23–26] can be used to analyze such cases. In particular, to good approximation there is a single source function that encodes observable features in the inflation potential [26] for canonical kinetic terms or the sound speed for noncanonical terms [27]. This function is also closely related to the source of corresponding bispectrum features [28]. In previous work, we studied the strong constraints on this function imposed by the precise and featureless measurements around the first acoustic peak through a low order principal components decomposition [29].

In this paper, we extend our previous analysis to a basis of 20 principal components for the source function of inflationary features. This basis is complete for models where the features vary no more rapidly than 10 per decade of the expansion or about 4 per efold during inflation. In Sec. II we review the GSR and principal components technique. In Appendix A, we describe numerical techniques used to reduce the computation time of the analysis. We test the validity of the GSR approximation in Appendix B. We present the results of the WMAP likelihood analysis in Sec. III. In Sec. IV we develop tests of single-field inflation and consider applications to specific classes of potentials. We discuss these results in Sec. V.

II. METHODOLOGY

We use the generalized slow roll (GSR) approximation and principal components to study features generated by single-field inflation. We refer the reader to Ref. [29] for details but provide a brief description here. Features arise from a single source function that describes the deviation from slow roll in the background (Sec. II A) which we can be decomposed into a basis of principal components that is complete for band-limited models sampled at a maximal rate per efold (Sec. II B).

A. Generalized slow roll

Under the GSR approximation, features in the curvature power spectrum are generated by a single source function of the background evolution of the inflaton ϕ

$$G'(\ln\eta) \equiv -2(\ln f)' + \frac{2}{3}(\ln f)'', \tag{1}$$

where

$$f = \frac{2\pi\dot{\phi}a\eta}{H}. \tag{2}$$

Primes here and below denote derivatives with respect to $\ln\eta$ where $\eta = \int_t^{t_{\rm end}} dt'/a(t')$ is the conformal time to the end of inflation and we take units where the reduced Planck mass $M_{\rm pl} = (8\pi G)^{-1/2} = 1$ as well as $c = 1$ and $\hbar = 1$.

In the ordinary slow-roll approximation, the curvature power spectrum is given by $\Delta^2_{\mathcal{R}} \approx f^{-2}$ since

$$\epsilon_H = \frac{1}{2}\left(\frac{\dot{\phi}}{H}\right)^2, \qquad \eta \approx \frac{1}{aH}. \tag{3}$$

In the GSR approximation, the curvature power spectrum is instead determined by features in the source function through

$$\ln\Delta^2_{\mathcal{R}}(k) \approx G(\ln\eta_{\rm min}) + \int_{\eta_{\rm min}}^{\eta_{\rm max}} \frac{d\eta}{\eta} W(k\eta)G'(\ln\eta) + \ln[1 + I_1^2(k)], \tag{4}$$

where integrating G' gives

$$G(\ln\eta) = -2\ln f + \frac{2}{3}(\ln f)'. \tag{5}$$

Here the nonlinear correction is given by

$$I_1(k) = \frac{1}{\sqrt{2}}\int_{\eta_{\rm min}}^{\eta_{\rm max}} \frac{d\eta}{\eta} X(k\eta)G'(\ln\eta). \tag{6}$$

We take $\eta_{\rm min} = 1$ Mpc and $\eta_{\rm max} = 10^5$ Mpc which more than covers the range observable to WMAP. The window functions

$$W(u) = \frac{3\sin(2u)}{2u^3} - \frac{3\cos(2u)}{u^2} - \frac{3\sin(2u)}{2u}, \qquad X(u) = \frac{3}{u^3}(\sin u - u\cos u)^2, \tag{7}$$

define the linear and nonlinear response of the curvature spectrum to G' respectively. Accuracy of the GSR approximation requires the nonlinear response, as quantified by I_1^2, to remain below order unity. We call this the GSR condition (see Appendix B).

B. Principal component analysis

The principal components of the WMAP7 Fisher matrix provide an efficient basis with which to decompose the source function (1)

$$G'(\ln\eta) = 1 - n_s + \sum_{a=1}^{N} m_a S_a(\ln\eta), \tag{8}$$

where the eigenfunctions S_a are constructed following Ref. [29] by sampling at a rate of 10 per decade in η or equivalently 4.3 per efold of inflation across $\eta = [1\text{–}10^5]$ Mpc with spline interpolation between the points. In terms of the width of features in the potential, this limit corresponds to $\Delta\phi \gtrsim \epsilon_H^{1/2}/4.3$. This rate is sufficient to capture models that describe the glitches in the WMAP7 power spectrum (see Sec. IV for a discussion of the limitations imposed by the sampling).

The amplitudes m_a then can be incorporated into a Markov Chain Monte Carlo (MCMC) likelihood analysis of the WMAP data. As described in Appendix A we slightly modify the original approach [29] to improve the convergence properties of the MCMC analysis. Since a constant G' described by n_s is equivalent to tilt in the curvature spectrum and $G(\ln\eta_{\rm min})$ is equivalent to a normalization parameter we replace them with effective parameters $\bar{G}'$ and A_c. Specifically $\bar{G}'$ is an average of G' for $30 < \eta/\text{Mpc} < 400$ and A_c is the normalization of the temperature power spectrum C_ℓ^{TT} at the first peak $\ell = 220$ relative to a fiducial choice that fits the WMAP7 data. From these two phenomenological parameters we can derive constraints for the tilt n_s and curvature power spectrum normalization A_s (see Appendix A).

Since a signal-to-noise analysis shows that 20 out of the 50 principal components are required for a complete representation of the WMAP data at our bandlimit [29], we choose $N = 20$ for our analysis. These first 20 principal components are shown in Fig. 1. Note that the first 10 components resemble local Fourier modes around $\eta \approx 10^2$ Mpc where the well-constrained first acoustic peak gets its power. It is not until components 11–20 that horizon scale features at low multipole or 10^3–10^4 Mpc are represented.

We use the MCMC method to determine joint constraints on the 20 PC amplitudes and cosmological parameters

$$p_\mu = \{m_1, \ldots, m_{20}, A_c, \bar{G}, \tau, \Omega_b h^2, \Omega_c h^2, \theta\}. \quad (9)$$

Here τ is the reionization optical depth, $\Omega_b h^2$ is the physical baryon density, $\Omega_c h^2$ is the physical dark matter density and θ is 100 times the angular size of the sound horizon at recombination.

The MCMC algorithm samples the parameter space evaluating the likelihood $\mathcal{L}(\mathbf{x}|\mathbf{p})$ of the data $\mathbf{x}$ given each proposed parameter set $\mathbf{p}$ (e.g. see [30,31]). The posterior distribution is obtained using Bayes' theorem,

$$\mathcal{P}(\mathbf{p}|\mathbf{x}) = \frac{\mathcal{L}(\mathbf{x}|\mathbf{p})\mathcal{P}(\mathbf{p})}{\int d\boldsymbol{\theta}\, \mathcal{L}(\mathbf{x}|\mathbf{p})\mathcal{P}(\mathbf{p})}, \quad (10)$$

where $\mathcal{P}(\mathbf{p})$ is the prior probability density. We place non-informative top hat priors on all parameters in Eq. (9). To ensure the validity of the GSR approximation we set the prior to zero if I_1 exceeds a maximum value of

$$I_{1,\max} = \max|I_1(k)| \quad (11)$$

at any k. As shown in Appendix B, a value of $I_{1,\max} = 1/\sqrt{2}$ is sufficient to ensure accuracy of the GSR approximation.

Figure 2 shows the maximal contribution to I_1 per unit amplitude deviation in each of the first 20 principal components. The higher PCs actually produce a slightly smaller response largely because the frequency of the oscillations in Fig. 1 begins to exceed that of the nonlinear response function $X(k\eta)$. Thus a prior of $I_{1,\max} = 1/\sqrt{2}$ actually allows high PC components to reach order unity and $|G'|$ to reach ~ 4 or greater.

The MCMC algorithm generates random draws from the posterior distribution. We test convergence of the samples to a stationary distribution that approximates the joint posterior density $\mathcal{P}(\mathbf{p}|\mathbf{x})$ by applying a conservative Gelman-Rubin criterion [32] of $R - 1 < 0.01$ across four chains. We use the code CosmoMC [33] for the MCMC analysis [34].

For the WMAP7 power spectrum data [35], we use the optimized approximate likelihood from Ref. [29]. In addition, we utilize data from the BICEP (Background Imaging

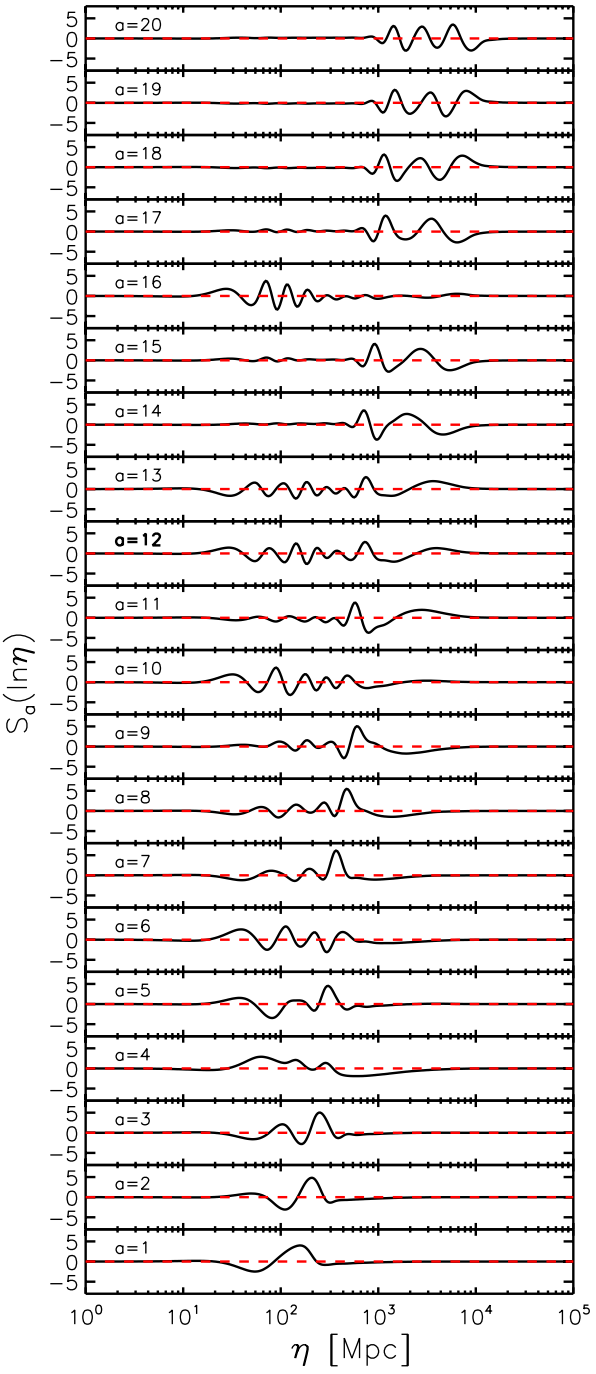

FIG. 1 (color online). The first 20 principal components of the GSR source G' [see Eq. (8)] as a function of conformal time to the end of inflation, in order of increasing variance from bottom to top. 20 PC components suffice to represent inflationary features observable to WMAP that vary no more rapidly than $\sim 1/4$ of an efold. Here and below, dashed red lines represent power law conditions with zero amplitude in the PC components.

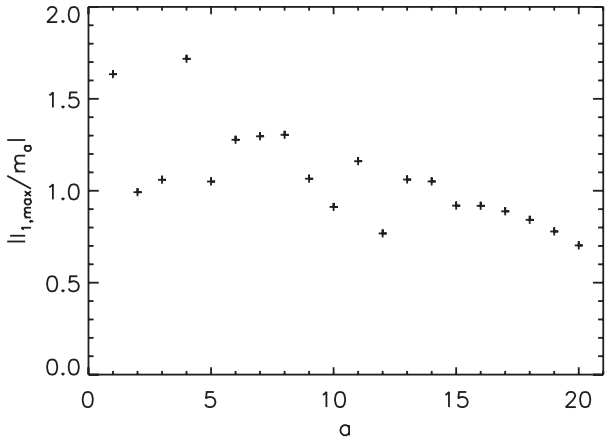

FIG. 2. Sensitivity of the nonlinearity parameter $I_{1,\max}$ (see Eq. (11)) to the amplitude of the first 20 PCs considered individually. This parameter must be less than order unity for the GSR approximation to be accurate, and we typically place a prior of $I_{1,\max} < 1/\sqrt{2}$.

of Cosmic Extragalactic Polarization) and QUAD (QU Extragalactic Survey Telescope at Degree Angular Scale Interferometer) experiments which include polarization constraints [36,37]. We calculate the CMB power spectra without incorporating gravitational lensing and the default sparse sampling in ℓ (accuracy$_{\rm boost} = 1$). We correct for these approximations in postprocessing by importance sampling as described in Appendix A before presenting the results in the next section. The main effect is a $\sim 0.5\sigma$ upwards shift in the $\Omega_b h^2$ posterior to compensate the smoothing effect of lensing.

In order to ensure that models are compatible with a reasonable cosmology we add non-CMB constraints from the UNION2 (a supernova type Ia compilation) [38], the SHOES (Supernova H_0 for the Equation of State) $H_0 = (74.2 \pm 3.6)$ km/s/Mpc measurement [39] and a big bang nucleosynthesis constraint of $\Omega_b h^2 = 0.022 \pm 0.002$ [40]. These data mainly constrain the energy density components of the universe rather than the inflationary initial conditions. We call the combination of CMB and external data the "all data" analysis. We address the impact of the $I_{1,\rm max}$ prior and the non-CMB data in Sec. III B below.

III. MCMC RESULTS

In this section, we present the results of the Markov Chain Monte Carlo analysis in the principal component (PC) space of the GSR source function. We discuss the results of our fiducial all-data analysis in Sec. III A and address the impact of priors and non-CMB data in Sec. III B.

A. All Data

For our fiducial results we use the all-data combination of CMB and external data described in the previous section. To establish a baseline for the PC results we start with the $m_a = 0$ power law (PL) case, $\Delta^2_{\mathcal{R}} = A_s(k/k_p)^{n_s-1}$. Table I gives the mean, standard deviation of the posterior probabilities, and the maximum likelihood (ML) parameter values for the power law model.

For the PC analysis, we take 20 components and a nonlinearity top hat prior of $I_{1,\rm max} < 1/\sqrt{2}$ (see Sec. II B). Table II gives the parameter constraints as well as the maximum likelihood PC model (left columns).

The improvement in the ML PC model over the ML power law model is $2\Delta \ln\mathcal{L} = 17$ for 20 extra parameters and so is not statistically significant in and of itself. Of course, specific inflationary models may realize this improvement with a smaller set of physical rather than phenomenological parameters (see Sec. IV B), and so it is interesting to examine more closely the origin of this improvement.

The main improvement comes from $\ell \le 60$ in the TT part of the WMAP likelihood with a $2\Delta \ln\mathcal{L} = 11.9$. We shall see in Sec. IV A that these improvements are largely associated with known features in the WMAP temperature power spectrum.

TABLE I. Power law (PL) parameter results: means, standard deviations (left subdivision of columns) and maximum likelihood values (right subdivision of columns) with CMB data (WMAP7 + BICEP + QUAD) and all data (+ UNION2 + H_0 + BBN) in a flat universe. H_0 and Ω_Λ constraints are derived from the other parameters.

Parameters	All Data		CMB Only	
$100\Omega_b h^2$	2.241 ± 0.048	2.233	2.231 ± 0.051	2.229
$\Omega_c h^2$	0.1101 ± 0.0040	0.1098	0.1110 ± 0.0051	0.1116
θ	1.0398 ± 0.0022	1.0397	1.0394 ± 0.0022	1.0394
τ	0.089 ± 0.014	0.086	0.087 ± 0.015	0.085
n_s, $1 - \bar{G}'$	0.9669 ± 0.9882	0.9649	0.9620 ± 0.0078	0.9622
$\ln[10^{10} A_s]$	3.0808 ± 0.0332	3.0733	3.0770 ± 0.0338	3.0746
H_0	71.23 ± 1.74	71.23	70.70 ± 2.32	70.40
Ω_Λ	0.738 ± 0.0198	0.739	0.732 ± 0.027	0.730
$-2\ln\mathcal{L}$	8140.06		7608.39	

In terms of the principal components, the improvements are localized in only a few of the 20 parameters. Figure 3 plots these m_a constraints and ML values. Most of the components are consistent with zero at the $\sim 1\sigma$ level. Components m_{17}–m_{20} are constrained in part by the $I_{1,\rm max}$ prior not just the data.

As in the 5 PC analysis of [29], the single most discrepant parameter between the PL and PC cases is m_4 corresponding to a feature centered around $\eta \sim 300$ Mpc and resembling a local running of the tilt. Figure 4 shows the posterior probability distributions of the parameters. An m_4 value as extreme as the power law value of $m_4 = 0$ is disfavored at 98.2% CL compared with 94.8% for 5 PCs and WMAP7 alone. The increase in significance by a fraction of a σ arises because of the correlation between m_4 and the higher principal components. Perhaps more importantly, freedom in the higher PCs allows large m_4 without the need to make large adjustments to the cosmological parameters that would violate non-CMB constraints. On the other hand, one event out of 20 showing a 98% exclusion is not that unlikely.

The poorly constrained $a > 10$ modes allow large amplitude deviations and in fact even marginally prefer them. This explains why including the higher components can change results on the lower components. Large amplitude deviations in the high order components make the modes no longer statistically independent as they would be for infinitesimal deviations. Still the correlation remains relatively small. For example $R_{4a} = \mathrm{Cov}(m_4, m_a)/\sigma_{m_4}\sigma_{m_a}$ reaches 0.4 only for one mode, m_5, with more typical correlations in the ± 0.1–0.2 range.

The next most significant deviations are in m_9 (with a value of $m_9 = 0$ disfavored at the 89.6% CL) and m_{18} (with a value of $m_{18} = 0$ disfavored at the 91.8% CL). These results are also consistent with the PL null hypothesis of

TABLE II. 20 principal component (PC) parameter results: means, standard deviations (left subdivision of columns) and maximum likelihood (ML) values (right subdivision of columns). Fiducial results are for all data and nonlinearity prior $I_{1,\max} = 1/\sqrt{2}$, left columns, with variations shown in center and right columns. Parameters $n_s - \Omega_\Lambda$ are derived from the chain parameters. The difference in likelihood $2\Delta \ln L$ is given for the ML values and taken with respect to the corresponding PL maximum likelihood model in Table I.

Parameters	All Data $I_{1,\max} = 1/\sqrt{2}$		All Data $I_{1,\max} = 1/2$		CMB Only $I_{1,\max} = 1/\sqrt{2}$	
$100\Omega_b h^2$	2.279 ± 0.107	2.227	2.282 ± 0.107	2.410	2.160 ± 0.159	2.110
$\Omega_c h^2$	0.1127 ± 0.0055	0.1101	0.1126 ± 0.0056	0.1100	0.1297 ± 0.0142	0.1338
θ	1.0411 ± 0.0030	1.0402	1.0411 ± 0.0030	1.0417	1.0395 ± 0.0032	1.0381
τ	0.086 ± 0.016	0.096	0.088 ± 0.016	0.091	0.082 ± 0.016	0.072
$\bar{G}'$	0.0122 ± 0.0268	0.0055	0.0191 ± 0.0248	0.0213	0.0186 ± 0.0283	0.0221
$\ln[10^{10} A_c]$	0.0032 ± 0.0117	0.0036	0.0032 ± 0.0122	0.0098	0.0051 ± 0.0122	0.0056
m_1	0.0048 ± 0.0073	0.0060	0.0025 ± 0.0071	0.0068	0.0021 ± 0.0078	0.0009
m_2	0.0152 ± 0.0122	0.0163	0.0120 ± 0.0122	0.0109	0.0086 ± 0.0137	0.0104
m_3	-0.0120 ± 0.0181	-0.0042	-0.0140 ± 0.0179	-0.0085	-0.0151 ± 0.0191	-0.0161
m_4	0.0427 ± 0.0190	0.0460	0.0327 ± 0.0171	0.0481	0.0455 ± 0.0195	0.0583
m_5	0.0198 ± 0.0256	0.0050	0.0168 ± 0.0249	0.0486	0.0165 ± 0.0272	0.0165
m_6	-0.0156 ± 0.0325	-0.0089	-0.0142 ± 0.0328	-0.0166	0.0062 ± 0.0377	-0.0120
m_7	-0.0061 ± 0.0354	-0.0015	-0.0060 ± 0.0333	-0.0060	-0.0174 ± 0.0383	-0.0324
m_8	0.0278 ± 0.0486	0.0285	0.0403 ± 0.0464	0.0431	0.0174 ± 0.0505	-0.0061
m_9	-0.1239 ± 0.0731	-0.1436	-0.0970 ± 0.0670	-0.1458	-0.1319 ± 0.0770	-0.1184
m_{10}	0.0336 ± 0.0609	0.0219	0.0282 ± 0.0602	0.0462	0.0150 ± 0.0647	0.0441
m_{11}	0.0759 ± 0.0908	0.0225	0.0599 ± 0.0847	0.0364	0.0591 ± 0.0966	0.1339
m_{12}	-0.0917 ± 0.1027	-0.1604	-0.0702 ± 0.0946	-0.1477	-0.1100 ± 0.1076	-0.2137
m_{13}	-0.0947 ± 0.1129	-0.1895	-0.0764 ± 0.1036	-0.1577	-0.0506 ± 0.1194	-0.2300
m_{14}	0.1116 ± 0.1616	0.2069	0.0561 ± 0.1450	0.2126	0.1507 ± 0.1714	0.2103
m_{15}	-0.0199 ± 0.2042	0.0617	0.0191 ± 0.1864	-0.0091	-0.0255 ± 0.2152	0.0686
m_{16}	0.1006 ± 0.0975	0.1318	0.0837 ± 0.0964	0.1102	0.1481 ± 0.1043	0.0772
m_{17}	-0.1253 ± 0.2688	-0.1953	-0.1094 ± 0.2326	-0.1302	-0.0575 ± 0.2833	-0.1376
m_{18}	-0.5089 ± 0.2938	-0.6131	-0.3322 ± 0.2475	-0.3798	-0.4894 ± 0.3083	-0.6610
m_{19}	0.2239 ± 0.3773	0.2737	0.1524 ± 0.3028	0.1785	0.2406 ± 0.3878	0.5228
m_{20}	-0.0742 ± 0.4070	0.0011	-0.2472 ± 0.3173	-0.1789	-0.1265 ± 0.4065	-0.0113
n_s	1.0299 ± 0.0671	1.1296	1.0075 ± 0.0515	1.0535	1.0191 ± 0.0672	1.0823
$\ln[10^{10} A_s]$	3.0387 ± 0.0582	3.0358	3.0446 ± 0.0573	3.0654	3.0684 ± 0.0626	3.0726
H_0	71.03 ± 2.28	71.22	71.08 ± 2.28	73.28	63.86 ± 5.88	61.35
Ω_Λ	0.730 ± 0.026	0.739	0.731 ± 0.026	0.750	0.614 ± 0.105	0.588
$2\Delta \ln L$	16.85		14.26		17.2	

$m_a = 0$, given that there are only 3 events out of 20 where tests of that model exceed the ~90% CL.

We can get further insight on the origin of these constraints by examining the maximum likelihood (ML) models. Figure 5 show temperature and polarization power spectra of the ML PL (red dashed lines) and PC (thick solid curve) models, respectively. The poorly constrained $a > 10$ modes create fluctuations in the low order multipoles which marginally fit features in the data better such as the low quadrupole and glitch at $\ell \sim 20$–40. These large amplitude modes require small amplitude low order PC variations in order to compensate the broadband residual effects they have. This can be seen by decomposing the difference between the ML PL and PC models into contributions from the various parameters (see Fig. 6). Removing the large m_{10}–m_{20} components from the model not only removes the low ℓ oscillations but also creates broadband deviations, especially at $\ell \lesssim 40$, that are compensated by a combination of small amplitude changes in m_1–m_5 and effective tilt $\bar{G}'$.

B. Robustness tests

In order to test the robustness of the fiducial results of the last section, we run separate MCMC chains with different choices for the nonlinearity prior and data sets.

We first examine the impact of our $I_{1,\max}$ prior by reanalyzing the all-data case with $I_{1,\max} = 1/2$ instead of $1/\sqrt{2}$ (see Table II). The main impact of tightening the prior is on m_{18}–m_{20} as is expected from Fig. 3. These components mainly affect the low ℓ multipoles. In spite of this fact the prior on $I_{1,\max}$ has very little impact on the behavior of favored models at low ℓ. In Fig. 7, we show the maximum likelihood model with the stronger $I_{1,\max}$ prior. Even at low ℓ the differences are much smaller than cosmic variance. In particular the posterior distribution of power in

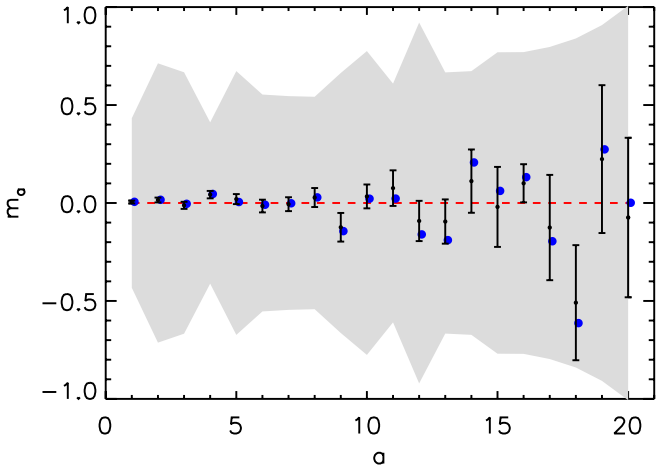

FIG. 3 (color online). Constraints on the 20 PC amplitudes from the all-data analysis with an $I_{1,\max} < 1/\sqrt{2}$ prior (gray band). The black points are the mean values of m_a and the error bars correspond to their 1σ error. The only significant deviation from the $m_a = 0$ PL expectation (red dashed line) is $m_4 = 0.0427 \pm 0.0190$. Only m_{17}–m_{20} are significantly prior limited. The maximum likelihood model is shown as blue points.

the quadrupole moment for models in the chain shown in Fig. 8 differ negligibly.

Some of this robustness in the low multipole moments is due to the impact of the non-CMB data. Without the external data, the quadrupole distribution extends to smaller quadrupole moments due to the ability to reduce the integrated Sachs-Wolfe effect by lowering the cosmological constant in the absence of constraints on the acceleration of the expansion (see Fig. 8). In this case the data may prefer more extreme inflationary models that further lower the quadrupole that are excluded by our nonlinearity prior on $I_{1,\max}$ [13].

The main impact on parameters of removing the non-CMB data is to allow a wider range in $\Omega_c h^2$ (see Table II). In contrast to the 5 PC analysis [29], this wider range though has little impact on the PC parameters. In particular the higher order PC components allow compensation of the effects of m_4 across the acoustic peaks without the need to vary $\Omega_c h^2$ substantially. For similar reasons, we expect our flatness prior to have little impact on the PC results aside from weakening the constraints on Ω_Λ and $\Omega_c h^2$ and small shifts of the location of features in G' with the angular diameter distance degeneracy.

IV. APPLICATIONS

Here we discuss applications of the fiducial 20 PC analysis of Sec. III A. In Sec. IV A we place constraints on and devise tests of slow-roll and single-field inflation in a model-independent manner. Alternately, as a complete observational basis for efold band-limited models, the PC analysis places constraints on any such model that satisfies

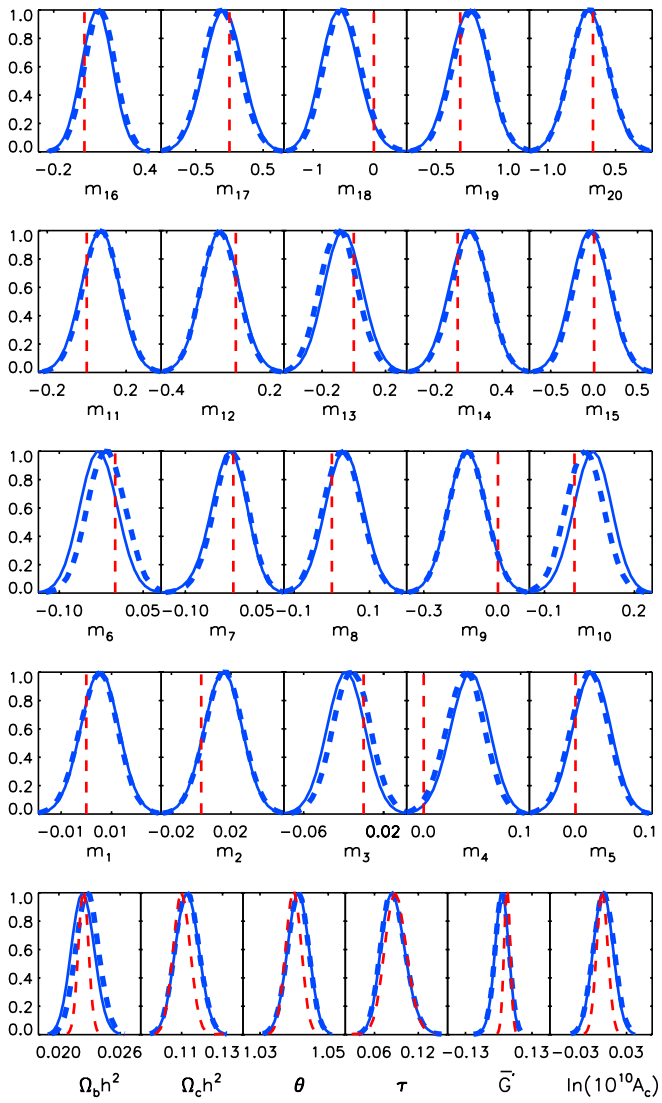

FIG. 4 (color online). Posterior parameter probability distributions from the all-data analysis in a flat universe with $I_{1,\max} = 1/\sqrt{2}$. Dashed lines represent the posteriors with approximations for the low ℓ polarization likelihood and C_ℓ accuracy used to run the MCMC (see Appendix); solid lines represent posteriors corrected by importance sampling. Red dashed lines represent corrected posteriors for power law models. Distributions here and below are arbitrarily normalized to their maximum value.

the GSR condition. We use running of the tilt and a step in the inflaton potential as example test cases in Sec. IV B.

A. Testing slow-roll and single-field inflation

Bounds on the PC components can be thought of as functional constraints on G' itself across the observed range from WMAP. These in turn limit features in the inflaton potential $V(\phi)$ through the approximate relation [26]

$$G'(\ln\eta) \approx 3\left(\frac{V_{,\phi}}{V}\right)^2 - 2\frac{V_{,\phi\phi}}{V}. \qquad (12)$$

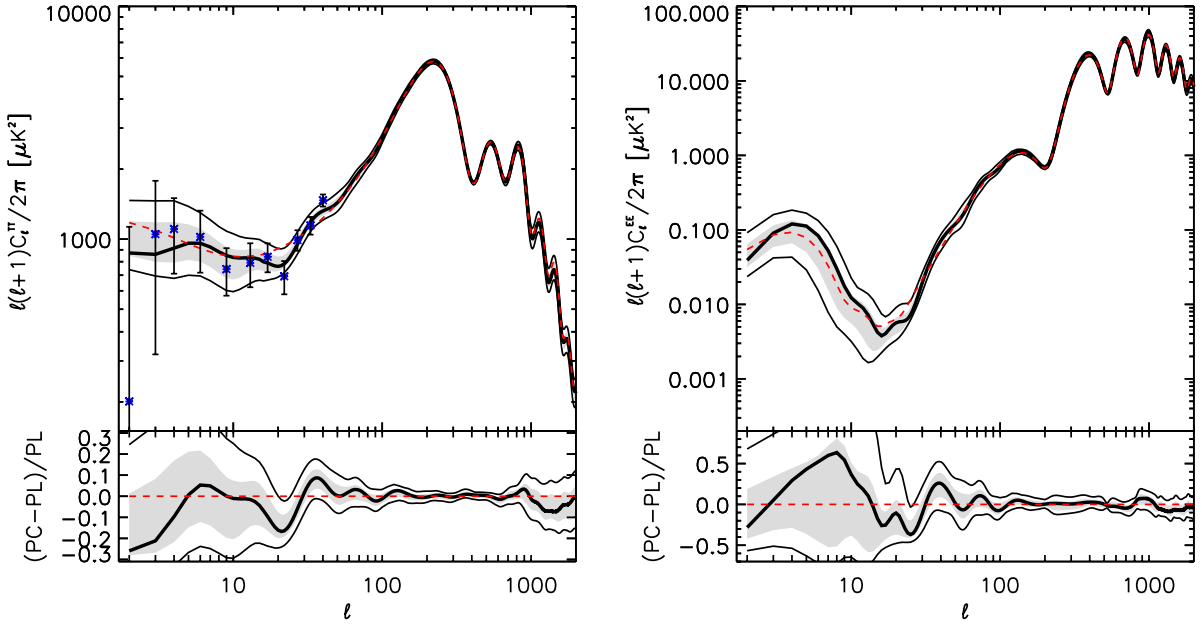

FIG. 5 (color online). The temperature (left) and E-mode polarization (right) power spectra posterior using the all-data PC constraints and a prior of $I_{1,\max} = 1/\sqrt{2}$. The shaded area encloses the 68% CL region and the upper and lower curves show the upper and lower 95% CL limits. The maximum likelihood (ML) model is shown as the thick black central curve, and the power law ML model is shown in red dashed lines. The blue points with error bars show the 7-year WMAP measurements.

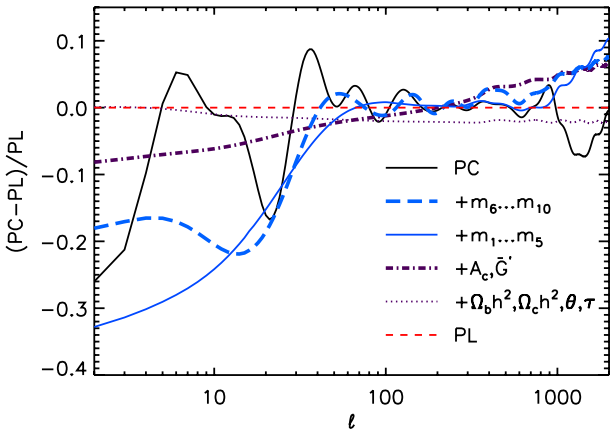

FIG. 6 (color online). Parameter decomposition of the temperature power spectrum difference between the power law (PL) and PC maximum likelihood (ML) models shown in Fig. 5 (bottom panel). The curves include cumulative changes in parameters between the models starting with the cosmological parameters, adding the normalization A_c and effective tilt $\tilde{G}'$, $m_1 \ldots m_5$, etc. until the full PC ML parameters are utilized.

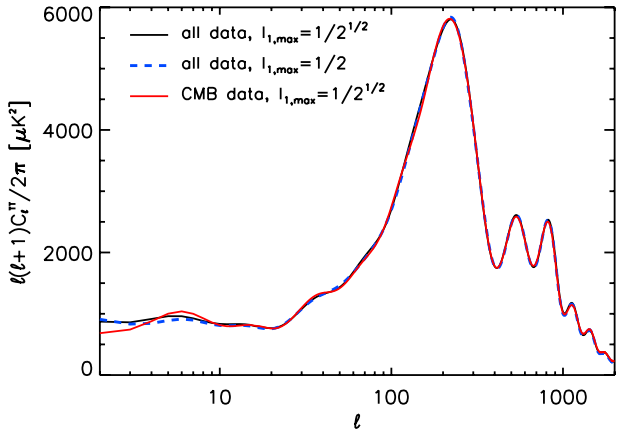

FIG. 7 (color online). Comparison of the maximum likelihood models of the three MCMCs of Table II: the all-data analysis with $I_{1,\max} = 1/\sqrt{2}$ (black curve), all-data with $I_{1,\max} = 1/2$ (blue curve), and CMB data with $I_{1,\max} = 1/\sqrt{2}$ (red curve). The smallness of the differences indicates robustness of our results to the priors and external data sets.

If the inflaton carries noncanonical kinetic terms then the relationship is modified to include variations in the sound speed [27].

Since the PC decomposition only represents features in G' across the observable domain, one should consider the constraints on the m_as as defining a PC filtered version of G':

$$G'_{20}(\ln\eta) = \sum_{a=1}^{20} m_a S_a(\ln\eta). \tag{13}$$

Any significant deviation from zero of this function would indicate a violation of ordinary slow roll. We can extract the posterior probability of G'_{20} by considering its values on a continuous set of samples of η as derived parameters.

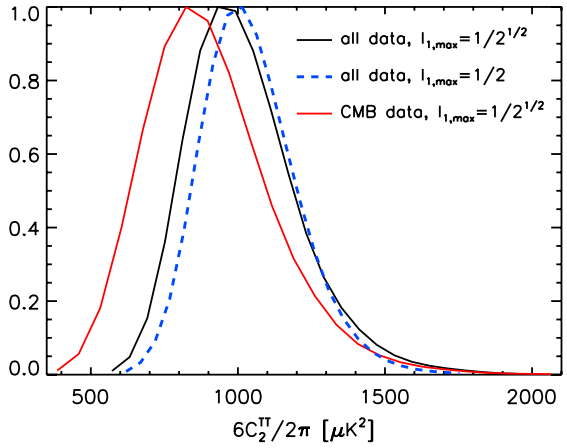

FIG. 8 (color online). The temperature quadrupole power C_2^{TT} posterior distribution for the all-data analysis with $I_{1,\max} = 1/\sqrt{2}$ (black curve), all-data with $I_{1,\max} = 1/2$ (blue curve), and CMB data with $I_{1,\max} = 1/\sqrt{2}$ (red curve). Without external data to constrain the cosmological constant, the quadrupole can be lowered by reducing the integrated Sachs-Wolfe effect.

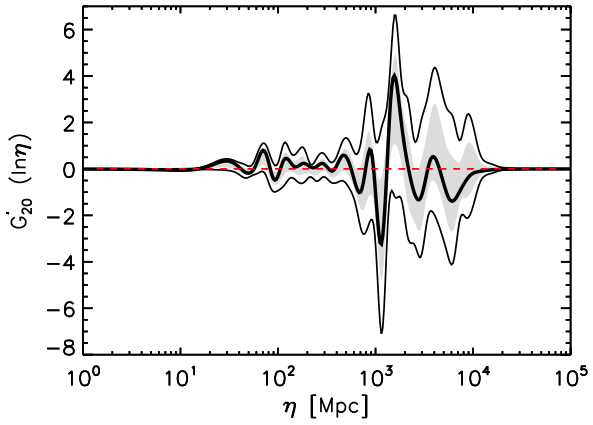

FIG. 9 (color online). The 20 PC filtered G' posterior from the fiducial all-data analysis and $I_{1,\max} = 1/\sqrt{2}$ as a prior. The shaded area encloses the 68% CL region and the upper and lower curves show the upper and lower 95% CL limits. The maximum likelihood is shown as the thick black central curve, and the power law ML model is shown in red dashed lines.

In Fig. 9 we plot both the ML model and the 68% and 95% posterior bands. Note that $G'_{20} = 0$ lies within the 95% CL regime for all η. These functional constraints differ from a full reconstruction of G' in that the PCs filter out deviations at $\eta < 20$ Mpc and $\eta > 10^4$ Mpc as well as deviations that are too high frequency to satisfy our bandlimit.

In the well-constrained regime of $30 \lesssim \eta/\mathrm{Mpc} \lesssim 400$ constraints are both tight and consistent with $G'_{20} = 0$. Only nearly zero mean high frequency deviations are allowed in this regime. Nonetheless, the poorly constrained m_{10}–m_{20} components allow, but do not strongly prefer, large oscillatory features between $10^3 \lesssim \eta/\mathrm{Mpc} \lesssim 10^4$. In fact $G'_{20} = 0$ lies noticeably outside the 68% CL bands only for the dip and bump between 1000–2000 Mpc and a bump at 70–100 Mpc.

We can associate the most significant features with the corresponding effects on the observable power spectra themselves. Figure 5 shows the 68% and 95% range in the power spectra posterior. The 1000–2000 Mpc feature in fact corresponds to the $\ell = 20$–40 dip and bump in the temperature power spectrum. The 70–100 Mpc feature corresponds to a glitch at $\ell \sim 600$–700 [14,15]. While the $\eta \gtrsim 10^4$ Mpc regime is limited by our priors on the amplitude of deviations through $I_{1,\max}$ we have shown that the data do not favor a feature corresponding to a low quadrupole $\ell = 2$ unless acceleration constraints are omitted (see Sec. III B).

Finally, we can examine the posterior distributions of the E-mode polarization. These predictions are not significantly constrained by the polarization data sets employed. Instead these distributions are limited mainly by the common origin of the temperature and polarization spectra from single-field inflation. These serve as predictions for future measurements. For example, the low significance features in the temperature power spectrum predict corresponding ones in the E-mode polarization which have yet to be measured and can be used to test the hypothesis of their inflationary origin at substantially higher joint significance [41]. In particular, one expects a $\sim 26\%^{+13\%}_{-17\%}$ enhancement in the EE power spectrum at $\ell = 39$ and a $\sim -37\%^{+17\%}_{-3\%}$ deficit around $\ell = 25$. The skew distribution in the latter case reflects the difficulty in constructing models with low power out of the principal components rather than the data disfavoring such models. Models that actually explain the low TT power at $\ell = 25$ predict low EE power as well.

Even in the acoustic regime where the polarization predictions are tight and do not suggest the presence of features, these predictions are of interest. If future observations violate them, then not only will slow-roll inflation be falsified but all single-field inflationary models, including those with sound speed variations, as long as they satisfy our weak prior constraint on acceptable models: the efold bandlimit and small GSR nonlinearity $I_{1,\max} < 1/\sqrt{2}$. Such a violation might indicate other degrees of freedom breaking the relationship between the temperature and polarization fields, e.g. isocurvature modes in multifield inflation or trace amounts of cosmological defects. For $\ell \lesssim 30$ violation could alternately indicate a more complicated reionization scenario [41].

Currently these bounds and tests apply to the $\ell < 800$ regime measured by WMAP but will soon be extended by high resolution ground based experiments and Planck.

B. Constraining inflationary models

We can also apply the model-independent PC analysis to any specific set of models that satisfy the GSR condition

$I_{1,\max} < 1/\sqrt{2}$ and bandlimit of features no sharper than about $1/4$ efold. To place constraints on the parameters of a model, one projects the source function G' of the model onto the principal components

$$m_a = \frac{1}{\ln\eta_{\max} - \ln\eta_{\min}} \int_{\eta_{\min}}^{\eta_{\max}} \frac{d\eta}{\eta} S_a(\ln\eta) G'(\ln\eta) \quad (14)$$

as a function of parameters and compares the result to the joint posterior probability distributions of the components. Likewise one can construct G'_{20} from the result and compare it with Fig. 9.

In fact, the means $\bar{m}_a$ and covariance matrix $\mathbf{C}$ of the components m_a extracted from their joint posterior form a simple but useful representation. From these, one can construct a χ^2 statistic

$$\chi^2 = \sum_{a,b=1}^{20} [(m_a - \bar{m}_a)\mathbf{C}^{-1}_{ab}(m_b - \bar{m}_b)], \quad (15)$$

or the likelihood $\mathcal{L} \propto \exp(-\chi^2/2)$ under a multivariate Gaussian approximation to the posteriors. For example the ML PC model gives an improvement of $\Delta\chi^2 = -15.36$ over PL to be compared with $-2\Delta \ln L = -16.85$.

As a simple illustration of a concrete model, consider a linear deviation in G'

$$G'(\ln\eta) = 1 - n_0 + \alpha \ln(\eta/\eta_0). \quad (16)$$

The curvature power spectrum for this model has a local tilt of

$$\frac{d\ln\Delta^2_{\mathcal{R}}}{d\ln k} = n_0 - 1 + \alpha \ln\left(\frac{k\eta_0}{C}\right) - \frac{\alpha\pi}{\sqrt{2}} \frac{I_1}{1 + I_1^2}, \quad (17)$$

where $C = e^{7/3-\gamma_E}/2 \approx 2.895$ and

$$I_1 = \frac{1}{\sqrt{2}}\left[\frac{\pi}{2}(1 - n_0 - \alpha \ln k\eta_0) + 1.67\alpha\right]. \quad (18)$$

For $|n_0 - 1| \ll 1$ and $|\alpha| \ll 1$, the I_1 term contributes negligibly and the model gives a linear running of the tilt [29].

The 20 PC components are a linear function of α given explicitly by

$$m_a(\alpha) = \frac{\alpha}{\ln\eta_{\max} - \ln\eta_{\min}} \int_{\eta_{\min}}^{\eta_{\max}} \frac{d\eta}{\eta} S_a(\ln\eta) \ln(\eta/\eta_0). \quad (19)$$

In Fig. 10 we show an example with $\alpha = -0.026$ and compare the original linear G' to the PC filtered G'_{20}. The filter introduces features at low and high η that are not present in the actual source. Note that a Fisher analysis of sensitivity to α reveals that most of the signal-to-noise should lie in the m_4 component [29] which carries the most significant deviations from zero in the data.

The χ^2 analysis with all data implies $\alpha = -0.039 \pm 0.019$. We can compare this result to a direct MCMC analysis with α as a parameter constructed from 20 PCs:

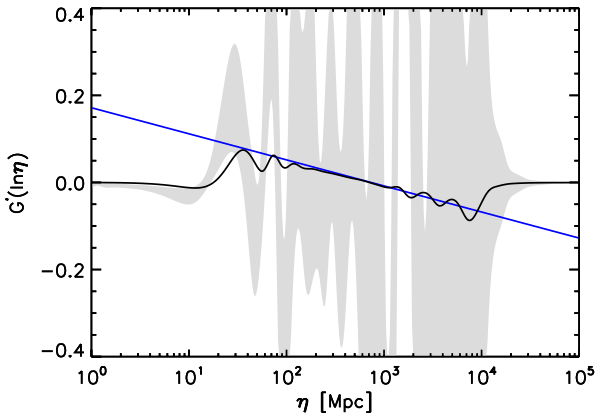

FIG. 10 (color online). A model with a linear deviation in G' with slope $\alpha = -0.026$ (and arbitrary offset) is shown as the blue curve. The 20 PC filtered source G'_{20} (in black lines) is compared with the input linear G' model. 20 PCs captures all of the observable information in α. These models are compatible with the 68% CL region (shaded) for G'_{20} from the fiducial all-data analysis.

$\alpha = -0.027 \pm 0.021$. Thus the simple χ^2 approximation captures the information on α in the 20 PC posterior to $\sim 0.5\sigma$.

We can further test the completeness of the 20 PC decomposition of α by going to 50 PCs. In this case $\alpha = -0.026 \pm 0.023$ showing that 20 PCs completely describe the observable properties of α. In fact, 5 PCs are enough to describe the observable properties of α in this case; a direct MCMC analysis gives $\alpha = -0.026 \pm 0.020$. Figure 11 shows that the full posterior distributions of α for these cases are indistinguishable within the errors. We also show the simple χ^2 approximation which is shifted by $\sim 0.5\sigma$ as expected.

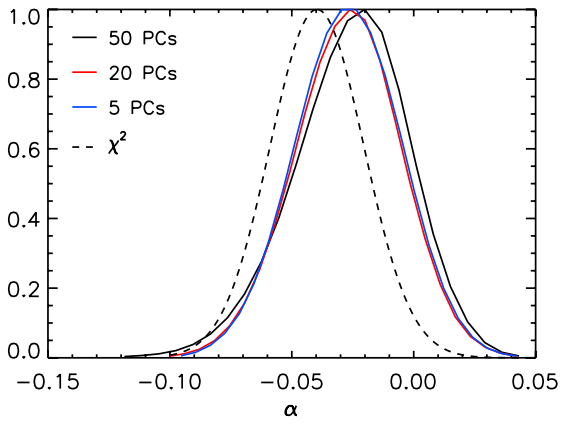

FIG. 11 (color online). Posterior probability distribution of α from a direct MCMC analysis constructed from 50 PCs (black/solid curve), 20 PCs (red curve), and 5 PCs (blue curve). The distribution from the χ^2 approximation is shown in black/dashed curve.

The posterior distributions are skewed to negative values of α. For example the ML model of the 50 PC chain has $\alpha = -0.021$ to be compared with a mean of -0.026. For large negative α, the linear G' model no longer matches a running of the tilt due to the I_1 terms in Eq. (18). In Fig. 12, we show an example with $n_0 = 0.96$ and $\eta_0 = 145$ Mpc for $\alpha = dn_s/d\ln k = -0.09$ and -0.02. While the α model closely matches constant $dn_s/d\ln k$ for the smaller value, it produces substantially less deviations at high and low k. This bias explains the difference between constraints on the linear α model and running of the tilt found in [29]. For example, with the same data sets and priors running of the tilt gives $dn_s/d\ln k = -0.018 \pm 0.019$. Note that the ML $\alpha = -0.021$ from the 50 PC chain is consistent with this constraint.

Another example is the step potential which has been employed to explain the glitches in the power spectrum at $\ell \approx 20$–40

$$V(\phi) = \frac{1}{2}m^2\phi^2\left[1 + c\tanh\left(\frac{\phi - \phi_s}{d}\right)\right]. \quad (20)$$

For simplicity, we fix $\phi_s = 14.668$ so that the feature appears at the correct position to explain the glitches with the convention that $\eta = 20$ Mpc is the comoving horizon scale 50 efolds before the end of inflation. Although we set the smooth part of the potential to correspond to an $m^2\phi^2$ model with $m = 7.126 \times 10^{-6}$ for the projection onto PCs, in the analysis we retain the freedom to adjust the amplitude and tilt as usual. This leaves us with 2 additional parameters c and d to control the amplitude and width of the step.

The constraints on (c, d) from the χ^2 approximation are shown in Fig. 13 (top panel). Note that the crude χ^2 analysis correctly picks out the favored parameters which can explain the glitches [41]. The minimum χ^2 model is $c = 0.0015$, $d = 0.026$ and is favored over the PL $m_a = 0$ (or $c = 0$) model by $\Delta\chi^2 = -10.2$. Although the χ^2 analysis assumes that the joint posterior in m_a is a multivariate Gaussian, it does not make that assumption for parameter probabilities. With the distorted shape of the confidence region, the contours of the 68% area of the probability distribution corresponds to $\Delta\chi^2 = 2.5$, 95% contour to 8.6 and 99.7% contour to 13.3, compared with the more stringent 2.3, 6.2 and 11.6 obtained for Gaussian distributions in (c, d). Here and below we take a prior of $d > 0.005$ due to our bandlimit of $1/4$ efold (see below).

We again compare this with a full analysis of the joint 20 PC posteriors. As in the case of α, the projection onto the two-dimensional $m_a(c, d)$ space leaves us with too few samples in the original 20 PC chain to reliably extract the posterior via importance sampling. We instead run a direct MCMC analysis on the 20 PC description with $m_a(c, d)$. These results are shown in Fig. 13 in blue lines. The maximum likelihood model has $c = 0.0016$, $d = 0.025$ and is favored over PL $m_a = 0$ (or $c = 0$) by

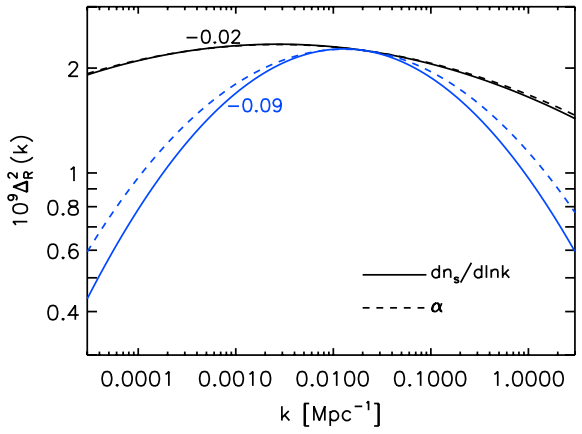

FIG. 12 (color online). Initial curvature power spectrum of a model with running of the tilt ($dn_s/d\ln k = -0.02, -0.09$, solid curves) compared to a model with a linear deviation in G' ($\alpha = -0.02, -0.09$, dashed curves). For the -0.02 case, the two models are similar whereas for -0.09 the running of the tilt model has larger deviations from scale free conditions at low and high k.

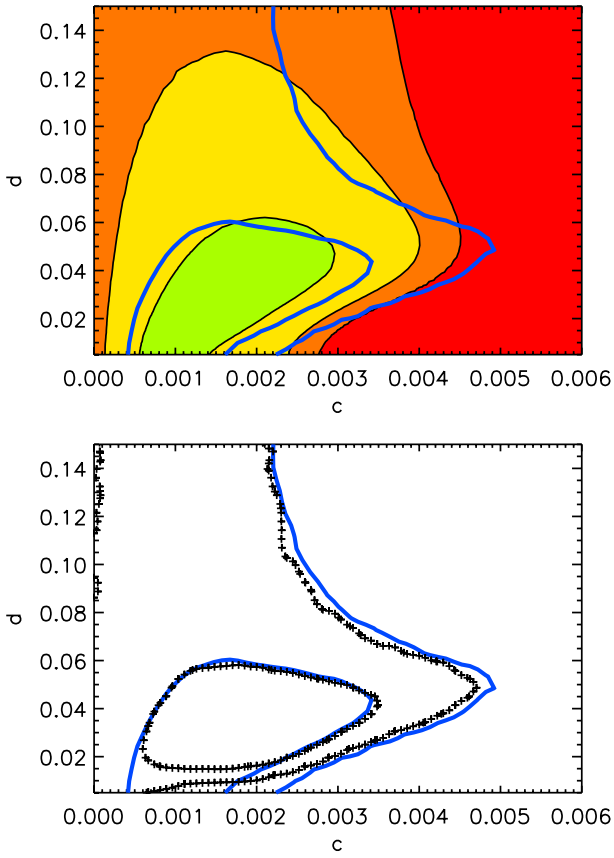

FIG. 13 (color online). Constraints on the step potential model parameters c (height of step) and d width of step. Top panel: the χ^2 approximation (black curves) compared to the full 20 PC posterior (blue curves). Bottom panel: constraints from the 20 PCs posterior (blue curves) compared to a direct GSR calculation of the model (black points).

$2\Delta \ln L = 9.1$. These values are fully consistent with the simple χ^2 analysis. This improvement is a substantial fraction of the total of 17 available to the 20 PCs from Table II and is achieved with 3 parameters: c, d and implicitly ϕ_s, the location of the step.

The filtered G'_{20} source for both the ML and minimum χ^2 model are shown in Fig. 14 and are consistent with the posteriors of the fiducial all-data analysis. Furthermore, the χ^2 analysis correctly picks out the best-fit region and qualitatively recovers its distorted shape. The main difference is that the confidence region is slightly underestimated.

Finally, we test the completeness of the 20 PC description of the step model by conducting a separate MCMC with the full function G' directly (see Appendix B, Eqs. (B10)–(B13) for details). The maximum likelihood model has $c = 0.0021$, $d = 0.029$ and is favored over PL by $2\Delta \ln L = 9.5$ As shown in Fig. 13 (bottom panel), the main difference is that the models are more tightly constrained at $d < 0.01$. The features in G' span less than $\sim 1/4$ of an efold for these models and consequently the 20 PC decomposition is not complete. In Fig. 15 (top panel) we show a model with $d = 9.2 \times 10^{-3}$ and $c = 4.6 \times 10^{-4}$ represented by the full function G' (in black lines) compared to its 20 PCs description (in blue/dashed curves). The fractional difference between these two constructions is shown in the bottom panel. In such models, the oscillations in the temperature power spectrum continue to higher ℓ, in this case $\ell \sim 100$, and are not allowed by the data.

This example shows that the main limitation of the 20 PC analysis is that it is too conservative for models with high frequency structure in the source: such models tend to be in conflict with the data in ways not represented by the principal components.

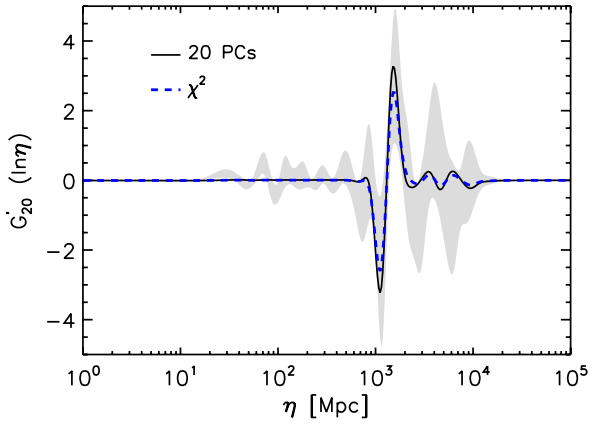

FIG. 14 (color online). The ML model of the step potential from the χ^2 approximation is shown in blue dashed lines, and the ML model from the projection onto 20 PCs [$m_a(c, d)$] is shown in black lines. The step potential model captures the main feature seen in the fiducial all-data analysis (shaded 68% CL area).

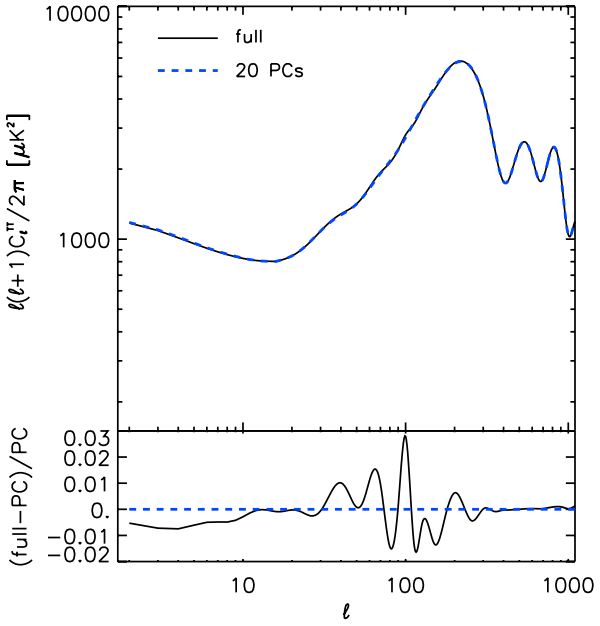

FIG. 15 (color online). Top panel: step potential model with width $d = 9.2 \times 10^{-3}$ and height $c = 4.6 \times 10^{-4}$ represented by the full source function G' (in black lines) compared to its 20 PC description (in blue/dashed lines). Bottom panel: fractional difference between the full GSR description and its 20 PC decomposition. The oscillations at $\ell \sim 100$ are not captured by the 20 PCs.

V. DISCUSSION

We have conducted a complete study of constraints from the WMAP7 data on inflationary features beyond the slow-roll limit. Using a principal component basis that accommodates order unity features as fine as $1/10$ of a decade across more than two decades of the inflationary expansion, we find no significant deviations from slow roll. Although one component shows a deviation at the 98% CL, it cannot be considered statistically significant given the 20 components tested. The maximum likelihood PC parameters only improves $2\Delta \ln L$ by 17 for the 20 parameters added.

On the other hand, specific inflationary models may access this improvement with fewer physical parameters. Most of the improvement comes from fitting features in the temperature power spectrum at multipoles $\ell \leq 60$ with the known glitch at $20 \leq \ell \leq 40$ comprising a large fraction. We have illustrated this fact by taking two parameters of the well-known step model represented in the 20 PC space.

From our analysis, we also extract predictions for the corresponding features in the polarization power spectrum that can be used to test their inflationary origin independently of a specific choice for the inflaton potential (cf. [41]). In particular, one expects a $\sim$26% enhancement in the EE power spectrum at $\ell = 39$ and a $\sim$37% deficit around $\ell = 25$ if the temperature features have an inflationary origin. Outside of the range of these low ℓ features,

the predictions are very precise and any violation of them in future observations would falsify single-field inflation independently of the potential.

Our constraints can also be used to test any single-field model that satisfies our conditions. Most of the information from the likelihood analysis is distilled in the means and covariance of the principal components themselves which we make publicly available [42]. Two models illustrate this encapsulation: a linear source model that approximates running of the tilt and a step potential model that fits the features at $\ell = 20$–40. A simple χ^2 analysis approximates the joint parameter posteriors despite its highly non-Gaussian form for the step parameters. This procedure greatly simplifies the testing of inflationary models with features in that parameter constraints on any model that satisfies our conditions can be simply approximated without a case-by-case likelihood analysis.

ACKNOWLEDGMENTS

We thank Peter Adshead and Mark Wyman for useful conversations. This work was supported by the KICP under NSF Contract No. PHY-0114422. W. H. was additionally supported by DOE Contract No. DE-FG02-90ER-40560 and the Packard Foundation.

APPENDIX A: MCMC OPTIMIZATION

1. Parameterization

We seek to define amplitude and tilt parameters for the MCMC that are nearly orthogonal to the PC parameters in order to improve the convergence properties of the MCMC chains.

A constant G' is equivalent to tilt n_s and hence PC components that have long positive or negative definite stretches become degenerate with tilt and cause problems for MCMC convergence. Instead of a constant tilt, we define a new chain parameter to be the average of G' across a narrower range that is better associated with the observables

$$\bar{G}' = \frac{1}{\ln\eta_2 - \ln\eta_1}\int_{\eta_1}^{\eta_2}\frac{d\eta}{\eta}G', \tag{A1}$$

where specifically, we choose $\eta_1 = 30$ Mpc and $\eta_2 = 400$ Mpc to roughly minimize the variance of $\bar{G}'$ in the chain (see Fig. 9).

Next, we replace the normalization parameter $G(\ln\eta_{\rm min})$ with

$$A_s \equiv \ln\Delta^2_{\mathcal{R}}(k_p), \tag{A2}$$

where in practice we choose $k_p = 0.05\ {\rm Mpc}^{-1}$.

The effective tilt and normalization parameters bring the model of the power spectrum from Eq. (4) to

$$\begin{aligned}\ln\Delta^2_{\mathcal{R}} = {} & \ln\left[A_s\left(\frac{k}{k_p}\right)^{-\bar{G}'}\right] + \sum_{a=1}^{N} m_a[\bar{W}_a(k) - \bar{W}_a(k_p)] \\ & + \ln\left[1 + \frac{1}{2}\left(\frac{\pi}{2}\bar{G}' + \sum_{a=1}^{N} m_a\bar{X}_a(k)\right)^2\right] \\ & - \ln\left[1 + \frac{1}{2}\left(\frac{\pi}{2}\bar{G}' + \sum_{a=1}^{N} m_a\bar{X}_a(k_p)\right)^2\right],\end{aligned} \tag{A3}$$

where

$$\begin{aligned}\bar{W}_a(k) &= \int_{\eta_{\rm min}}^{\eta_{\rm max}}\frac{d\eta}{\eta}W(k\eta)(S_a(\ln\eta) - \bar{S}_a), \\ \bar{X}_a(k) &= \int_{\eta_{\rm min}}^{\eta_{\rm max}}\frac{d\eta}{\eta}X(k\eta)(S_a(\ln\eta) - \bar{S}_a),\end{aligned} \tag{A4}$$

and

$$\bar{S}_a \equiv \frac{1}{\ln\eta_2 - \ln\eta_1}\int_{\eta_1}^{\eta_2}\frac{d\eta}{\eta}S_a. \tag{A5}$$

Note that we can recover the tilt n_s, equivalent to the average of $\bar{G}$ across the whole range $\eta_{\rm min}$ to $\eta_{\rm max}$, as

$$n_s = (1 - \bar{G}') + \sum_{a=1}^{20} m_a\bar{S}_a, \tag{A6}$$

and keep it as a derived parameter in the chain.

Given the oscillatory nature of the k-space response to the PC eigenfunctions through $\bar{W}_a$ and $\bar{X}_a$ and the geometric projection from k to angular multipole ℓ, normalization at a given k does not correspond simply to normalization at a given ℓ. Since the observations best constrain the amplitude of the temperature power spectrum near the first acoustic peak at $\ell \sim 220$ it is advantageous to use an ℓ-space normalization in the MCMC and then transform back to A_s.

Let us define a phenomenological parameter A_c which renormalizes the angular power spectra as

$$C_\ell^{XY} = e^{\ln A_c}\frac{C_{220}^{TT\rm fid}}{\tilde{C}_{220}^{TT}}\tilde{C}_\ell^{XY}. \tag{A7}$$

Here $C_{220}^{TT\rm fid}$ is the temperature power spectrum at the first peak of a fiducial model that fits the WMAP7 data. We use $C_{220}^{TT\rm fid} = 0.747\ \mu{\rm K}^2$. Thus if $A_c = 0$, $C_{220}^{TT} = C_{220}^{TT\rm fid}$ regardless of the PC parameters.

We can recover constraints on the k-space normalization by considering A_s as a derived parameter. If we compute the original $\tilde{C}_\ell^{XY}$ with the $A_s = A_s^{\rm fid}$ of the fiducial model, then the true A_s is given by

$$\ln A_s = \ln A_c + \ln(C_{220}^{TT\rm fid}/\tilde{C}_{220}^{TT}) + \ln A_s^{\rm fid}. \tag{A8}$$

In summary, we replace the parameters n_s and $G(\ln\eta_{\rm min})$ with $\bar{G}'$ and A_c in order to reduce parameter degeneracies that would otherwise inhibit chain convergence.

2. Likelihood corrections

To speed up the calculation of the WMAP and other CMB likelihoods we employ three approximations when running the chains. Firstly, we use a fitting function for the low ℓ WMAP7 polarization likelihood as described in [29]. Secondly, we calculate the CMB power spectra with gravitational lensing artificially turned off. Thirdly, we use the default ℓ-space sampling of CAMB that is designed for smooth underlying power spectra. Each of these approximations produce small errors in the likelihood evaluation that we can correct by importance sampling the chain.

The advantage of correcting these approximations in a postprocessing step is twofold. The chains may be thinned due to the high correlation between samples in the chain. Secondly, postprocessing elements of the thinned chains is embarrassingly parallel unlike the running of the original chain.

In practice, when we satisfy our convergence criterion described in the main text, we thin the chains by a factor of half of the correlation length. We have tested that with such thinning we reproduce the posteriors of the original chains. Next we compute the CMB power spectra of the thinned chains with lensing turned on and a higher ℓ-space sampling (CAMB "accuracy boost" 2). We use these high accuracy power spectra to correct the chain multiplicity for the change in the likelihood.

In Fig. 16 we show as an example the posteriors coming directly from power law (PL) chains (in blue/solid curves),

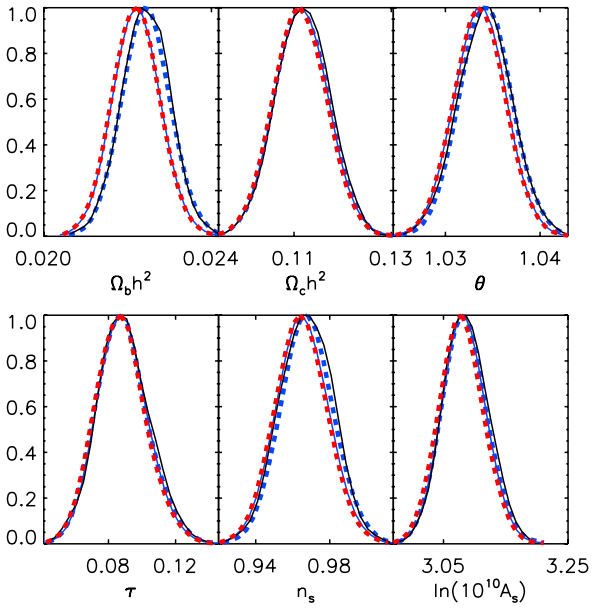

FIG. 16 (color online). Power law parameter posteriors from the approximations used to run the MCMC chain (in blue/solid curve), from an independent MCMC with no approximation (in black/solid curve), from the approximate chain with importance sampling correction (in blue/dashed curve), and from the approximate chain without lensing correction (in red/dashed curve).

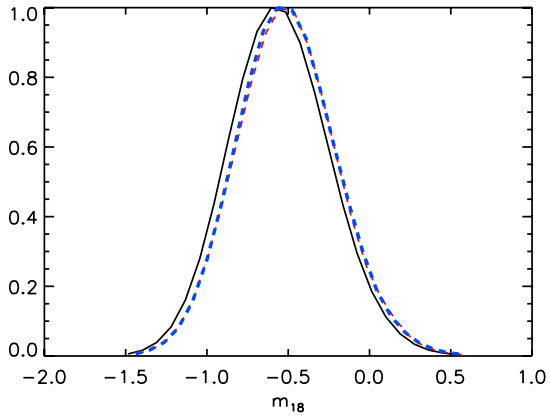

FIG. 17 (color online). The m_{18} posterior probability distributions from the approximations used to run the MCMC with all data and $I_{1,\max} = 1/\sqrt{2}$ (in black lines), from the approximate chain with importance sampling correction (in blue/dashed lines), and from the approximate chain without lensing correction (in red/dashed lines). m_{18} has the largest correction of the PC amplitudes which is still $\ll 1\sigma$ and dominated by the lensing correction.

the chains with all corrections (in blue/dashed lines) and finally all corrections but lensing (in red/dashed lines). These should be compared with results from a separate chain run with all the corrections turned on from the start (in black/solid lines). Importance sampling accurately models the impact of the small corrections for all parameters. The leading correction is on $\Omega_b h^2$ from lensing.

In Fig. 17, we show the impact of the corrections on the PC chain using m_{18} as an example with the largest correction. The correction on PC parameters is extremely small and again dominated by lensing.

APPENDIX B: GSR ACCURACY

To test the accuracy of the GSR approximation in the PC space, we need to consider the inverse problem: construct an inflationary model that matches a desired G' for which we can solve exactly for the curvature power spectrum.

In the forward direction, given an inflationary model we can compute the exact curvature spectrum by first evaluating the background behavior of the model through

$$g(\ln\eta) = \frac{f''}{f} - 3\frac{f'}{f} = \frac{3}{2}G' + \left(\frac{f'}{f}\right)^2, \tag{B1}$$

and then solving the equation

$$\frac{d^2y}{dx^2} + \left(1 - \frac{2}{x^2}\right)y = \frac{g}{x^2}y, \tag{B2}$$

where $x = k\eta$, subject to the usual Bunch-Davies initial conditions [23]. The curvature power spectrum is then given by

$$\Delta^2_{\mathcal{R}} = \lim_{x\to 0} x^2 \frac{|y|^2}{f^2}. \tag{B3}$$

Therefore to test the GSR approximation we first need to determine the function g that matches a given $G'(\ln\eta)$. Transforming variables to $r = f'/f$, we obtain from Eq. (B1)

$$r' - 3r = \frac{3}{2}G', \tag{B4}$$

which has the general solution

$$r = \frac{3}{2}\eta^3 \int \frac{d\tilde{\eta}}{\tilde{\eta}}\,\tilde{\eta}^{-3}G' + C\eta^3. \tag{B5}$$

Let us choose the integration constant

$$C = -\frac{3}{2}\int_{\eta_{\rm min}}^{\eta_{\rm max}} \frac{d\tilde{\eta}}{\tilde{\eta}}\,\tilde{\eta}^{-3}G', \tag{B6}$$

and assume G' vanishes outside this range. We then get

$$r = -\frac{3}{2}\eta^3 \int_{\eta}^{\eta_{\rm max}} \frac{d\tilde{\eta}}{\tilde{\eta}}\,\tilde{\eta}^{-3}G', \tag{B7}$$

for $\eta > \eta_{\rm min}$ and

$$r = -\frac{3}{2}\eta^3 \int_{\eta_{\rm min}}^{\eta_{\rm max}} \frac{d\tilde{\eta}}{\tilde{\eta}}\,\tilde{\eta}^{-3}G', \tag{B8}$$

for $\eta < \eta_{\rm min}$. With this numerical solution we construct g as

$$g = \frac{3}{2}G' + r^2. \tag{B9}$$

This suffices to specify the source for y in Eq. (B2). Finally, to get the curvature power spectrum we need f at some $\eta_{\rm lim} \ll k_{\rm max}^{-1}$. However since this quantity is independent of k, it is absorbed into our normalization definition. In Fig. 18, we take parameters from the all-data chain and use this technique to calculate the temperature power spectra of matching inflationary models exactly. Even for the model that saturates the $I_{1,\rm max} = 1/\sqrt{2}$ prior, the WMAP likelihood difference between the exact and GSR calculation is $|2\Delta \ln L| = 0.4$.

Using the step model chain from Sec. IV B, we can explore the accuracy of the GSR approximation as a function of $I_{1,\rm max}$ independently of the prior taken in the all-data analysis. Specifically, we take a model from the chain that defines G' and construct the matching full inflationary model as above.

Recall that to construct G', we solve for the background evolution of ϕ in the step potential of Eq. (20). This specifies the $m^2\phi^2$ model source through Eq. (1), which we call G'_m. To allow for a retilting of the spectrum, we add an extra constant parameter $\bar{G}'_p$ to the model source to form the full source

$$G'(\ln\eta; c, d, \bar{G}'_p) = G'_m(\ln\eta; c, d) + \bar{G}'_p. \tag{B10}$$

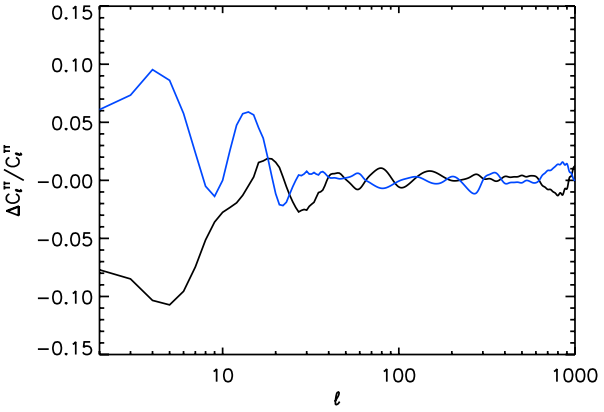

FIG. 18 (color online). Fractional difference in temperature power spectra between GSR and the exact inflationary solution for the maximum likelihood model from the all-data analysis (in black lines) as well as a model that saturates the prior $I_{1,\rm max} = 1/\sqrt{2}$ from the chain (in blue lines). For reference, the ML model has $I_{1,\rm max} = 0.66$.

The GSR approximation then tells us that the curvature spectrum is given by

$$\ln\Delta^2_{\mathcal{R}} = \ln\left[A_s\left(\frac{k}{k_p}\right)^{-\bar{G}'_p}\right] + I_m(k) - I_m(k_p) \tag{B11}$$

with

$$I_m(k) = \int_{\eta_{\rm min}}^{\eta_{\rm max}} \frac{d\eta}{\eta} W(k\eta) G'_m + \ln\left[1 + \frac{1}{2}\left(\frac{\pi}{2}\bar{G}'_p + \int_{\eta_{\rm min}}^{\eta_{\rm max}} \frac{d\eta}{\eta} X(k\eta) G'_m\right)^2\right]. \tag{B12}$$

In Fig. 19, we compare the impact of taking this power spectrum to a full inflationary calculation with matching

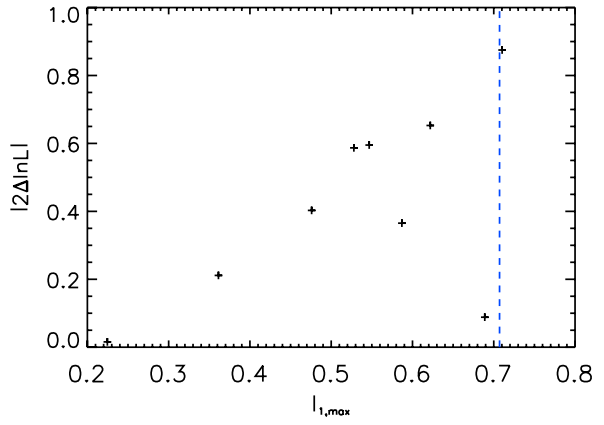

FIG. 19 (color online). Likelihood difference between the GSR solution and the full inflationary calculation of a series of step potential models as a function of $I_{1,\rm max}$. Models were chosen from the full GSR chain to be the maximum likelihood in a series of bins in step amplitude c. The maximal error is small below $I_{1,\rm max} = 1/\sqrt{2}$ (blue dashed line), the prior in the fiducial all-sky analysis.

source (B10) on the WMAP likelihood. For the full calculation of Eq. (B3), we take $\Delta^2_{\mathcal{R}}(k_p) = A_s$ to define the normalization f. Since $I_{1,\max}$ increases monotonically with c, we show models with maximum likelihood parameters in uniform bins of c. Note that the maximal error increases with $I_{1,\max}$ but does not exceed order unity at $I_{1,\max} < 1/\sqrt{2}$.

For reference, to compute a matching 20 PC representation as in Fig. 15 we take the amplitudes of the principal components from Eq. (14) and use Eq. (A1) to define

$$\bar{G}' = \bar{G}'_p + \frac{1}{\ln\eta_2 - \ln\eta_1}\int_{\eta_1}^{\eta_2}\frac{d\eta}{\eta}G'_m(\ln\eta). \quad \text{(B13)}$$

and keep the normalization A_s fixed.

[1] H. V. Peiris *et al.* (WMAP), Astrophys. J. Suppl. Ser. **148**, 213 (2003).
[2] W. Hu and T. Okamoto, Phys. Rev. D **69**, 043004 (2004).
[3] S. L. Bridle, A. M. Lewis, J. Weller, and G. Efstathiou, Mon. Not. R. Astron. Soc. **342**, L72 (2003).
[4] S. Hannestad, J. Cosmol. Astropart. Phys. 04 (2004) 002.
[5] S. M. Leach, Mon. Not. R. Astron. Soc. **372**, 646 (2006).
[6] D. Tocchini-Valentini, M. Douspis, and J. Silk, Mon. Not. R. Astron. Soc. **359**, 31 (2005).
[7] P. Mukherjee and Y. Wang, J. Cosmol. Astropart. Phys. 12 (2005) 007.
[8] M. Bridges, A. Lasenby, and M. Hobson, arXiv:astro-ph/0607404 [Mon. Not. Roy. Astron. Soc. (to be published)].
[9] A. Shafieloo and T. Souradeep, Phys. Rev. D **78**, 023511 (2008).
[10] H. V. Peiris and L. Verde, Phys. Rev. D **81**, 021302 (2010).
[11] G. Nicholson, C. R. Contaldi, and P. Paykari, J. Cosmol. Astropart. Phys. 01 (2010) 016.
[12] R. Nagata and J. Yokoyama, Phys. Rev. D **79**, 043010 (2009).
[13] C. R. Contaldi, M. Peloso, L. Kofman, and A. D. Linde, J. Cosmol. Astropart. Phys. 07 (2003) 002.
[14] L. Covi, J. Hamann, A. Melchiorri, A. Slosar, and I. Sorbera, Phys. Rev. D **74**, 083509 (2006).
[15] J. Hamann, L. Covi, A. Melchiorri, and A. Slosar, Phys. Rev. D **76**, 023503 (2007).
[16] J. E. Lidsey *et al.*, Rev. Mod. Phys. **69**, 373 (1997).
[17] I. J. Grivell and A. R. Liddle, Phys. Rev. D **61**, 081301 (2000).
[18] S. M. Leach and A. R. Liddle, Phys. Rev. D **68**, 123508 (2003).
[19] H. Peiris and R. Easther, J. Cosmol. Astropart. Phys. 10 (2006) 017.
[20] W. H. Kinney, E. W. Kolb, A. Melchiorri, and A. Riotto, Phys. Rev. D **78**, 087302 (2008).
[21] A. A. Starobinsky, JETP Lett. **55**, 489 (1992).
[22] J. A. Adams, B. Cresswell, and R. Easther, Phys. Rev. D **64**, 123514 (2001).
[23] E. D. Stewart, Phys. Rev. D **65**, 103508 (2002).
[24] J. Choe, J.-O. Gong, and E. D. Stewart, J. Cosmol. Astropart. Phys. 07 (2004) 012.
[25] K. Kadota, S. Dodelson, W. Hu, and E. D. Stewart, Phys. Rev. D **72**, 023510 (2005).
[26] C. Dvorkin and W. Hu, Phys. Rev. D **81**, 023518 (2010).
[27] W. Hu, Phys. Rev. D **84**, 027303 (2011).
[28] P. Adshead, W. Hu, C. Dvorkin, and H. V. Peiris, Phys. Rev. D **84**, 043519 (2011).
[29] C. Dvorkin and W. Hu, Phys. Rev. D **82**, 043513 (2010).
[30] N. Christensen, R. Meyer, L. Knox, and B. Luey, Classical Quantum Gravity **18**, 2677 (2001).
[31] A. Kosowsky, M. Milosavljevic, and R. Jimenez, Phys. Rev. D **66**, 063007 (2002).
[32] A. Gelman and D. Rubin, Stat. Sci. **7**, 452 (1992); available at http://projecteuclid.org/DPubS?service=UI=1.0=Display=euclid.ss/1177011136.
[33] A. Lewis and S. Bridle, Phys. Rev. D **66**, 103511 (2002).
[34] http://cosmologist.info/cosmomc.
[35] D. Larson *et al.*, Astrophys. J. Suppl. Ser. **192**, 16 (2011).
[36] H. C. Chiang *et al.*, Astrophys. J. **711**, 1123 (2010).
[37] M. L. Brown *et al.* (QUaD), Astrophys. J. **705**, 978 (2009).
[38] http://www.supernova.lbl.gov/Union.
[39] A. G. Riess *et al.*, Astrophys. J. **699**, 539 (2009).
[40] S. Burles, K. M. Nollett, and M. S. Turner, Astrophys. J. **552**, L1 (2001).
[41] M. J. Mortonson, C. Dvorkin, H. V. Peiris, and W. Hu, Phys. Rev. D **79**, 103519 (2009).
[42] http://background.uchicago.edu/wmap_fast.